nanomaterials

MDPI

Article

Improvement of the Interface between the Lithium Anode and a Garnet-Type Solid Electrolyte of Lithium Batteries Using an Aluminum-Nitride Layer

Wen Jiang [1], Lingling Dong [1], Shuanghui Liu [1], Bing Ai [1], Shuangshuang Zhao [2], Weimin Zhang [1], Kefeng Pan [1,*] and Lipeng Zhang [2,*]

[1] School of Chemistry and Chemical Engineering, Shandong University of Technology, Zibo 255049, China; wengejang@126.com (W.J.); donglingling202107@163.com (L.D.); shuanghuiliu2020@163.com (S.L.); aibing@sdut.edu.cn (B.A.); wmzhang@sdut.edu.cn (W.Z.)

[2] School of Materials and New Energy, South China Normal University, Shanwei 516600, China; 20219207@m.scnu.edu.cn

* Correspondence: xiaopandy@126.com (K.P.); zhanglipeng@sdut.edu.cn (L.Z.)

Abstract: The next generation of all-solid-state batteries can feature battery safety that is unparalleled among conventional liquid batteries. The garnet-type solid-state electrolyte $Li_7La_3Zr_2O_{12}$ (LLZO), in particular, is widely studied because of its high Li-ion conductivity and stability in air. However, the poor interface-contact between Li and the electrolyte (garnet) severely limits the development of solid electrolytes. In this study, we synthesize cubic phase $Li_{6.4}La_3Zr_{1.4}Ta_{0.6}O_{12}$ (LLZTO) using a secondary sintering method. In addition, a thin aluminum nitride (AlN) layer is introduced between the metal (Li) and the solid electrolyte. Theoretical calculations show that AlN has a high affinity for Li. Furthermore, it is shown that the AlN coating can effectively reduce the interface impedance between Li and the solid electrolyte and improve the lithium-ion transport. The assembled symmetric Li cells can operate stably for more than 3600 h, unlike the symmetric cells without AlN coating, which short-circuited after only a few cycles. The hybrid solid-state battery with a modified layer, which is assembled using $LiFePO_4$ (LFP), still has a capacity of 120 mAh g^{-1} after 200 cycles, with a capacity retention rate of 98%. This shows that the introduction of an AlN interlayer is very helpful to obtain a stable Li/solid-electrolyte interface, which improves the cycling stability of the battery.

Keywords: LLZTO; solid-state electrolytes; lithium/electrolyte interface; anode interface; lithium-ion battery

Citation: Jiang, W.; Dong, L.; Liu, S.; Ai, B.; Zhao, S.; Zhang, W.; Pan, K.; Zhang, L. Improvement of the Interface between the Lithium Anode and a Garnet-Type Solid Electrolyte of Lithium Batteries Using an Aluminum-Nitride Layer. *Nanomaterials* **2022**, *12*, 2023. https://doi.org/10.3390/nano12122023

Academic Editor: Christian M. Julien

Received: 6 May 2022
Accepted: 9 June 2022
Published: 12 June 2022

1. Introduction

The widespread use of electronic devices and the growing popularity of electric vehicles led to higher demands for the energy density of batteries. Unfortunately, a higher energy-density also tends to decrease battery safety [1–4]. Traditional liquid lithium-ion batteries use flammable organic electrolytes and diaphragms, which are prone to lithium dendrites piercing the diaphragm and causing a short-circuit inside the battery that can lead to a thermal runaway, fire, and even explosion. It is critical that battery safety is maintained when the energy density of the battery improves. Unfortunately, this is not an easy problem to solve, and this limits the development of conventional lithium-ion batteries [5–10]. All-solid-state batteries (ASSBs) can, in principle, solve the safety problem of conventional lithium-ion batteries by using a solid electrolyte instead of the organic diaphragm and liquid electrolyte of conventional liquid batteries. Moreover, ASSBs have several advantages such as high energy-density and excellent cycling performance [11–13]. Currently, all-solid-state batteries are intensively studied because they are promising candidates for the next generation of battery technology [14,15].

The key characteristic of ASSBs batteries is, of course, the solid-state electrolyte. Currently, solid state electrolytes are mainly divided into organic polymer solid-state electrolytes (OSSEs) and inorganic solid-state electrolytes (ISSEs) [16,17]. The OSSEs are widely studied. They include polyethylene oxide (PEO) [18], polyvinylidene fluoride (PVDF) [19], poly(vinylidene fluoride-co-hexafluoropropylene) (PVDF-HFP) [20], polyacrylonitrile (PAN) [21], and polymethyl methacrylate (PMMA) [22]. OSSEs usually have excellent processability, flexibility, safety, and good interface contact with electrodes [23,24]. However, the ionic conductivity of OSSEs is generally low ($<10^{-4}$ Scm^{-1}), both thermal and electrochemical stability is poor, and the suppression of lithium dendrites is unsatisfactory, which seriously limits their development [25].

ISSEs, on the other hand, include mainly lithium phosphorus oxynitride (LiPON) [26,27], perovskite [28], sulfide [29], and garnet [30]. LiPON solid-state electrolytes show excellent overall performance, but the required special sputtering process limits their large-scale development [31]. Perovskite-based structural materials have higher ionic conductivity at low temperatures than conventional electrolytes [32]. Their biggest disadvantage is that Ti^{4+} is reduced when it comes into contact with lithium [33]. Sulfide-based solid-state electrolytes have relatively high lithium-ion conductivity and low activation energy [34]. However, they are highly sensitive to air and prone to producing toxic H_2S. In addition, sulfide solid electrolytes are prone to react with lithium, which limits the doping of the lithium anode [35].

Compared to the solid-state electrolytes above, the garnet electrolyte $Li_7La_3Zr_2O_{12}$ (LLZO) has a higher ionic conductivity, a wider electrochemical stability window, and better stability in air [36], which makes it a promising candidate electrolyte for ASSBs. Although the LLZO electrolyte has many advantages, the ionic conductivity of the tetragonal phase is low at room temperature, and the cubic phase with its high ionic conductivity is difficult to stabilize at room temperature [37]. During the calcination process, doping with Al, Nb, Ta, and other elements is an effective method to stabilize the cubic phase at room temperature [38]. Secondly, the problem of poor contact between the garnet solid electrolyte and lithium limits the development of solid electrolytes. Typically, a buffer layer made of metals such as Au [39,40], Mg [41], Ge [42], Nb [39], Sn [43], as well as metal-oxide layers such as ZnO [44], SnO_2 [45], Al_2O_3 [46,47], can be introduced between the Li and the LLZO. This buffer layer can effectively reduce the interface impedance between Li and LLZO and strengthen the interface contact between Li and LLZO. It was previously thought that polishing LLZO in an inert gas would be effective in improving the interfacial contact between LLZO and the Li metal, but recent studies have shown that mechanical polishing actually creates an inert layer on the LLZO surface, and that short etching of LLZO with HCl in air can effectively remove the inert layer and thus release the intrinsic electrochemical activity of LLZO [48–50].

Moreover, Li_9Al_4 sites can be generated, in situ, on AlN nanoclusters with Li_3N to promote rapid migration of Li^+ ions and uniform plating/exfoliation [51,52]. In this study, we obtain Ta-doped $Li_{6.4}La_3Zr_{1.4}Ta_{0.6}O_{12}$ (LLZTO) using a secondary sintering method, and we successfully introduce a homogeneous AlN layer between Li and LLZTO to improve the affinity of the Li electrode with the solid electrolyte. Theoretical calculations show that AlN has a high affinity for Li, and AlN is also wettable for LLZTO. The experimental results show that the AlN coating confirms that not only can it effectively reduce the interface impedance between Li and solid electrolyte, but it can also facilitate the lithium-ion transport. The assembled symmetric Li cells can operate stably for more than 3600 h, unlike the symmetric cells without the AlN coating (which short-circuit after only a few cycles). The hybrid solid-state battery with the modified layer, which is assembled using $LiFePO_4$ (LFP), still has a capacity of 120 mAh g^{-1} after 200 cycles, with a capacity retention rate of 98%. This shows that the method of introducing an AlN interlayer is very effective to construct a stable Li solid-electrolyte interface and improve the cycling stability of the battery.

2. Materials and Methods

2.1. Preparation of Garnet LLZTO Electrolytes

Cubic garnet $Li_{6.4}La_3Zr_{1.4}Ta_{0.6}O_{12}$ (LLZTO) electrolyte was prepared using a conventional solid-state reaction. Stoichiometric amounts of La_2O_3 (Aladdin Inc., Shanghai, China, 99.99% purity), ZrO_2 (Aladdin Inc., Shanghai, China, 99.99% purity), Ta_2O_5 (Aladdin Inc., Shanghai, China, 99.99% purity), 1.2 wt% Al_2O_3 (Aladdin Inc., Shanghai, China, 99.99% purity), and 15 wt% excess of LiOH (Aladdin Inc., Shanghai, China, 98% purity) were used to compensate the loss of Li during the calcination. The starting materials were mixed with isopropanol and placed in a planetary ball-mill with small zirconia balls, at 600 rpm for 12 h for homogenization. The precursor powder was sintered in air at 900 °C for 12 h. Subsequently, the powder was ground via ball-milling for another 12 h at 600 rpm. Finally, the powder was pressed into 15 mm pellets under a pressure of 18 MPa and sintered at 1170 °C for 12 h in a muffle furnace. The pellets were covered by the mother powder to reduce lithium loss during sintering. The sintered pellets were mirror-polished well with 800, 1200, 1500, and 2000 grit SiC sandpaper, ultrasonically cleaned, dried, and stored in an argon-filled glovebox until further use.

2.2. Preparation of the AlN Mixed Interlayer

The AlN (Aladdin Inc., Shanghai, China, 99.5% purity) (Supplementary Figure S1) thin films were deposited on the polished LLZTO pellets via manual spot coating. The preparation process is shown in Figure 1. Firstly, AlN powder and PVDF were mixed, with a mass ratio of 9:1, and then ground well. Then, the solvent 1-Methyl-2-pyrrolidinone (NMP) was added and placed in a slurry machine at 2000 rpm for 15 min. The mixed slurry was ultrasonicated to ensure it is dispersed evenly. Finally, the mixed slurry was added, dropwise, to the surface of the LLZTO electrolyte sheet using a disposable pipette. After the slurry had been evenly dispersed, the coated electrolyte sheet was dried in a vacuum dryer at 60 °C for 24 h to obtain AlN-LLZTO. The required material for the symmetric cell was coated on the other side using the same method.

Figure 1. Schematic illustration of AlN coated LLZTO.

2.3. The DFT Method

All calculations were performed using the projector augmented wave (PAW) method in the framework of density functional theory (DFT), as implemented in the Vienna ab-initio Simulation Package (VASP) [53,54]. The generalized gradient approximation (GGA) and Perdew–Burke–Ernzerhof (PBE) exchange functional was used [55,56]. The plane-wave energy cutoff was set to 500 eV. The Monkhorst–Pack method with 2 × 2 × 1 k-meshes was employed for the Brillouin zone sampling of Li, AlN, and LLZTO. For the interface calculations with large supercells, we only needed the 2 × 2 × 1 k-mesh. The convergence criteria for the energy and force calculations were set to 10^{-5} eV·atom^{-1} and 0.01 eV·Å^{-1}, respectively. S2 provides details of the DFT method.

2.4. Assembly of Symmetric Cells and Hybrid Solid-State Full Cells

Symmetric cells and hybrid solid-state full cells were assembled using a standard 2032 cell-battery shell. Symmetric cells were assembled using two lithium disks (~0.6 mm thick and ~10.0 mm in diameter) attached to both sides of the AlN-modified LLZTO pellets (~0.8 mm thick and ~12.0 mm in diameter) to produce a sandwich structure. For

comparison, a symmetric cell without the modified layer was assembled at the same time. The $LiFePO_4$ (LFP) cathode was made by casting the carbon-coated $LiFePO_4$ powder, Ketjen Black (KB), and polyvinylidene fluoride (PVDF), with a weight ratio of 8:1:1 in NMP onto the Al foil. After drying in a vacuum oven at 60 °C, the obtained cathode film was punched into disks with a diameter of 12 mm. A drop of liquid electrolyte (~10 µL, 1.0 mol L^{-1} $LiPF_6$ in ethylene carbonate and diethyl carbonate (EC/DEC (volume ratio 1:1)) was added between the LFP cathode and the LLZTO pellets to improve the interface contact between the cathode and the solid electrolyte. The full cell was sealed inside a 2032 coin-battery housing. The battery assembly process was carried out in an Ar-filled glovebox.

Electrochemical impedance spectroscopy (EIS) measurements were performed with a Zennium electrochemical workstation (Zahner Inc., Berlin, Germany), an operating frequency range from 4 MHz to 10 Hz and an amplitude of 10 mV. The ionic conductivity of the LLZTO pellet was tested after sputtering Ag layers on both sides of the pellet, which serve as blocking electrodes. Constant current charge/discharge tests of full batteries were performed at various current densities (e.g., 1 C = 170 mA g^{-1}) in the voltage range of 4.0–2.5 V using Neware battery testers. The symmetric cells were tested at 30 °C.

2.5. Characterizations

The crystal structures of the samples were examined using X-ray diffraction (Rigaku Inc., Tokyo, Japan) with Cu Kα radiation (λ = 0.15418 nm). The scan range was 10–80° with a scan speed of 10°/min. Raman spectroscopy was performed with a Raman spectrometer (Horiba Inc., Paris, France). The morphology of the samples was observed with a scanning electron microscope (FEI Inc., Hillsboro, OR, USA), equipped with an energy-dispersive spectroscope (EDS).

3. Results

3.1. Characterization of LLZTO Solid Electrolyte Materials

The cubic-phase LLZTO solid electrolyte was synthesized using a secondary sintering method. Figure 2a shows the X-ray diffraction (XRD) patterns of the pre-sintered powder at 900 °C and the LLZTO powder prepared by sintering LLZTO dense pellets at 1170 °C. Both diffractograms are consistent with cubic garnet $Li_5La_3Nb_2O_{12}$ (PDF 80-0457), which indicates that the pure cubic LLZO pellets were produced as we expected. The shape of the XRD peak of the sample after sintering at 1170 °C is sharper, which suggests higher crystallinity of the sample. Figure 2b shows the Raman spectrum of the sintered LLZTO sample. The low-frequency region (<300 cm^{-1}) vibrational bands can be assigned to the LiO_6 octahedral unit ($96h_{Li2}$ position), while the middle-frequency region (300–550 cm^{-1}) vibrational bending modes can be assigned to the LiO_4 tetrahedral unit ($24d_{Li1}$ position). The high-frequency region (>550 cm^{-1}) bands correspond to the stretching mode of the ZrO_6 octahedral unit (16a position) [57]. The Raman spectra of tantalum-doped LLZO are consistent with the cubic phase of LLZO garnet reported in the literature [58,59]. The peaks at 625 and 720 cm^{-1} correspond to the band of the stretching mode of the Zr-O bond and the additional band of the Ta-O unit, respectively. The very strong Raman peak, which corresponds to the vibrational mode of $CO_3{}^{-2}$ and generally appears at 1090cm^{-1}, was not observed in LLZTO. This indicates that the pellets were free from Li_2CO_3 [60]. A cross-section SEM image of the sintered pellet is shown in Figure 2c and Figure S3. It can be seen that the particle shape of the sample, which was pre-sintered at 900 °C, is vein-like, and when the calcination temperature was 1170 °C, the grain size increased and showed a dense morphology. Furthermore, it is found that most grains are tightly packed. In some areas, the grain boundaries disappear due to grain amalgamation. The corresponding EDS mappings (Figure 2d) for the elements O, La, Zr and Ta from the cross-section SEM image (Figure 2c) further show that the localization of O, La, Zr, and doping ions Ta was uniformly distributed among the crystal grains. According to the EIS spectra (Figure S3), the semicircle for the high-frequency part comes from the total impedance comprising both bulk and grain boundary resistances. The tail at low frequency is caused by ion-blocking

Ag electrodes. The Li-ion conductivity of the LLZTO pellet, which can be derived from the low-frequency intercept, was calculated to be 2.7×10^{-4} S cm^{-1} at 25 °C. Figure 2e shows the Nyquist plots for the LLZTO pellet range from 25 to 60 °C. Clearly, the Li-ion conduction of the LLZTO pellet was increased at higher temperatures. The activation energy for Li-ion conduction is 0.28 eV, which was calculated using the Arrhenius equation (S5) and the Arrhenius plots in Figure 2f.

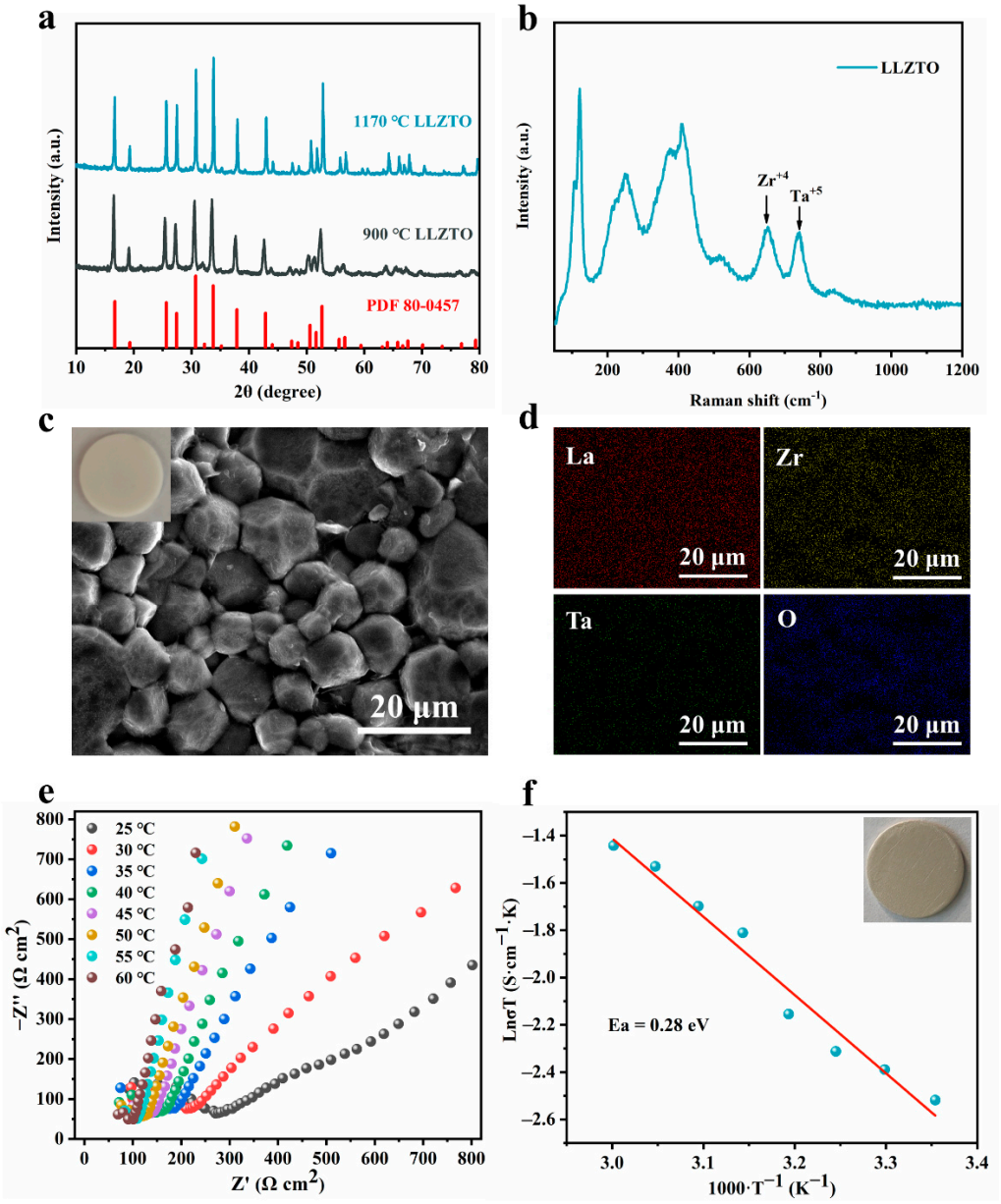

Figure 2. (**a**) The XRD pattern of the as-prepared LLZTO match the cubic structure well; (**b**) Raman spectra of the LLZTO; (**c**) cross-section SEM image of the LLZTO pellet, inset is a photo of an LLZTO pellet; (**e**) EIS profiles of the LLZTO electrolyte at different temperatures in the range 25–60 °C; (**f**) Arrhenius plots of the ionic conductivity for the LLZTO. Inset is a photo of Ag-LLZTO.

3.2. Characterization of AlN Modified LLZTO

Figure 3a shows the cross-section SEM of the as-prepared LLZTO interface with AlN layer. The thickness of the AlN hybrid coating is about 8 μm, and the hybrid coating of AlN and cross-linked PVDF is flexible and adheres effectively to the LLZTO surface. The AlN hybrid coating can wet the LLZTO interface and fill the cavities at the surface of the solid electrolyte, which improves the interface contact between lithium and the

solid electrolyte, and it facilitates ion transport. Figure 3b shows the EDS mapping of the modified AlN/LLZTO interface. It indicates that the AlN layer is in close contact with the LLZTO solid electrolyte sheet, and the AlN is distributed uniformly. As shown in Figure 3c, the poor contact between lithium and the non-interface modified LLZTO solid electrolyte leads to significant gaps between the two. The introduction of the AlN interlayer fills the cavities in the surface of the solid electrolyte. As shown in Figure 3d, the lithium metal and LLZTO are in close contact, and no cracks are found. This indicates that the AlN coating effectively enhances the interface contact, and the two-phase interface (now with good contact) can better promote the transport of ions.

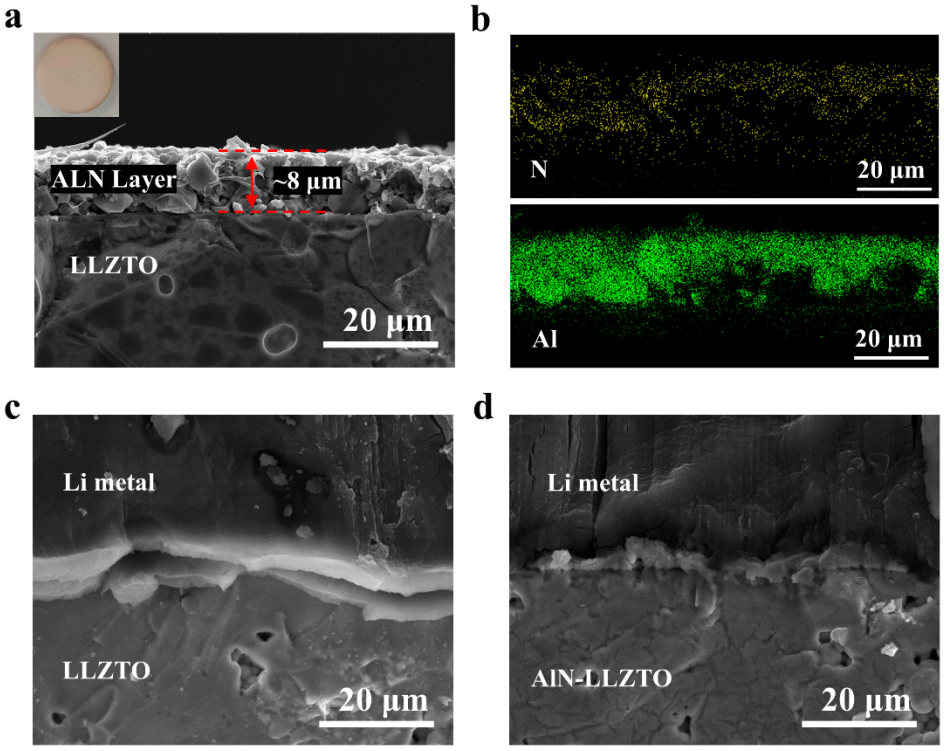

Figure 3. Cross section SEM image of the AlN-LLZTO (**a**), and the corresponding EDS mappings of N and Al (**b**). The inset is a photo of the AlN-LLZTO pellet. Cross-section SEM images of the Li/LLZTO interface (**c**) without- and (**d**) with AlN-interlayer.

3.3. Electrochemical Analysis of AlN Modified LLZTO

To evaluate the effect of the AlN film on the contact at the interface and the cycle stability, both the symmetric Li/AlN-LLZTO-AlN/Li cells and Li/LLZTO/Li cells were assembled using the same method. As shown in Figure 4a, the Nyquist plots for the symmetric cell of non-modified LLZTO and AlN-LLZTO exhibit one semicircle. This semicircle is assigned to the interface resistance. Considering the symmetry of the Li/LLZTO interfaces, the interface resistance of a single Li/LLZTO interface is 7.89 kΩ cm^2, while the interface resistance of LLZTO coated with AlN is reduced to 0.89 kΩ cm^2. To better understand this effect, the interaction of Li/LLZTO, Li/AlN, and AlN/LLZTO was studied using density functional theory (DFT) calculations. As shown in Figures 4b and S6, the interface formation energy of Li/LLZTO, AlN/LLZTO and Li/AlN are −0.024, −0.146, and −2.333 eV·$Å^{-2}$, respectively, implying the intrinsic capabilities of AlN to wet LLZTO. Additionally, AlN has the intrinsic ability to wet Li, and the mutually wettable interface facilitates the diffusion of ions. The AlN film can ensure tight contact of the Li/LLZTO interface and promote Li-ion transport. Furthermore, the critical current density (CCD) is an important indicator to determine whether the electrolyte electrode system can work stably at high current-densities. In the system with a Li electrode and the garnet solid electrolyte, the CCD reflects the barrier between the solid electrolyte and Li dendrites at high current

densities [61]. The Li/AlN-LLZTO-AlN/Li cells were measured at 30 °C, with a current density increase of 0.0625 mA cm^{-2} every 0.5 h from 0.12 mA cm^{-2} to 1.12 mA cm^{-2} for constant-current cycling. The solid line (red) in S7 indicates a sharp voltage fluctuation, around 0.4 mA cm^{-2}, from which it can be identified as a CCD of 0.4 mA cm^{-2}. However, the Li/LLZTO/Li cell was short-circuited at the beginning. The cycle performance of the symmetric Li-electrode cells was measured using galvanostatic charging and discharging (GCD) tests with a constant current at 30 °C. S8 shows that the Li/LLZTO/Li cell cannot cycle stably, and it short-circuits quickly due to the poor solid–solid contact interface. On the other hand, the Li/AlN-LLZTO-AlN/Li symmetric cell, after the introduction of AlN film, can cycle stably for more than 3600 h at 0.01 mA cm^{-2} (Figure 4c). This indicates that the introduction of the AlN film can improve the Li-electrode/electrolyte interface contact and facilitate the Li-ion transfer between the interfaces.

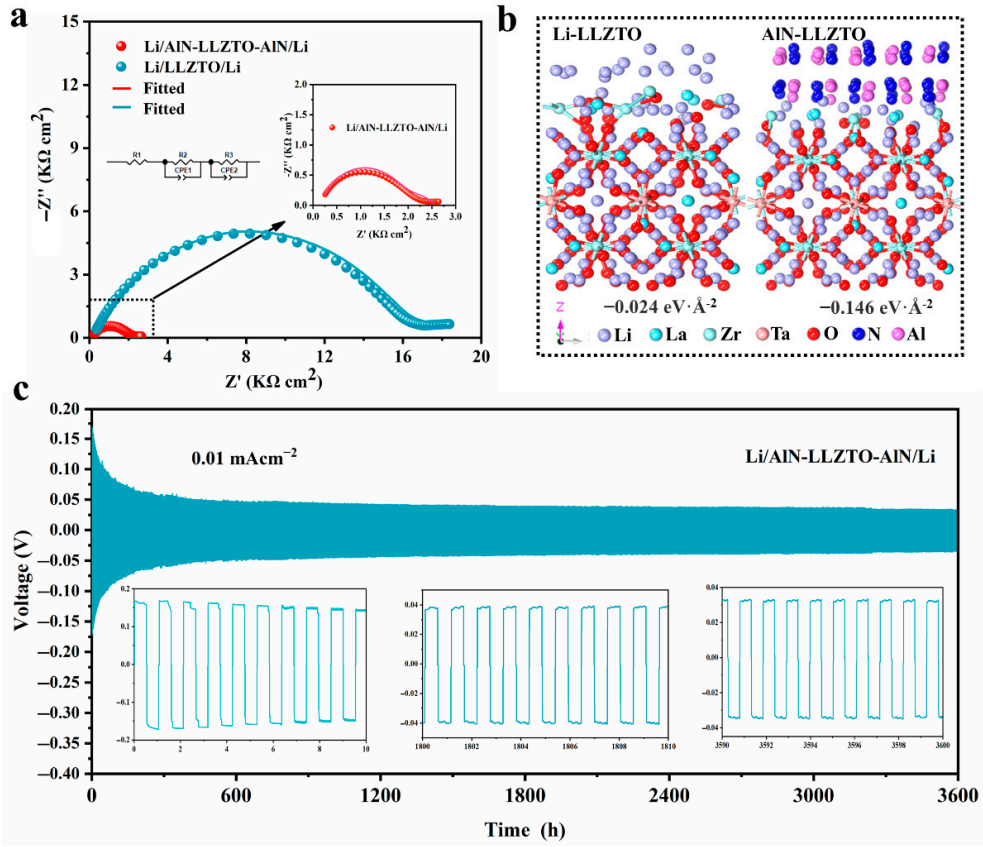

Figure 4. (**a**) Comparison of Nyquist plots of Li/AlN-LLZTO-AlN/Li and Li/LLZTO/Li at 30 °C; (**b**) DFT calculations of the interface formation energies for Li/LLZTO and AlN/LLZTO; (**c**) voltage profiles and details for the symmetric (Li/AlN-LLZTO-AlN/Li) cell for current densities of 0.01 mA cm^{-2} with 0.005 mAh cm^{-2}.

To confirm the availability of AlN-modified LLZTO in a lithium-ion battery, both Li/AlN- LLZTO/LFP and Li/LLZTO/LFP hybrid solid-state full cells were assembled and tested. Figure 5a shows a schematic diagram of the structure of the hybrid solid-state full cell. A tiny amount of the liquid electrolyte was introduced between the $LiFePO_4$ cathode and LLZTO electrolyte to wet the two-phase interface. Details of the preparation and assembly of the complete cell are provided in the Experimental section. The Nyquist plots of the hybrid solid-state Li/AlN-LLZTO/LFP and Li/LLZTO/LFP full cell were recorded. As shown in Figure 5b, each plot has a suppressed semi-circle in the high and medium frequency and a line in the low frequency. The turning points of the Li/LLZTO/LFP appear at ~1.47 Hz, where the values of the Z'-axis were evaluated with respect to the specific resistance of the total area (1010 Ω cm^2). The specific resistance of the total area dropped to 640 Ω cm^2 after the AlN film was introduced. Figure 5c shows the rate performance of

the Li/AlN-LLZTO/LFP and Li/LLZTO/LFP cell. The discharge capacities of Li/AlN-LLZTO/LFP are 132.4, 128.4, 119.9, 109.4 and 97.2 mA h g^{-1} at 0.1, 0.2, 0.5, 1 C and 2 C, respectively. The rate performance of Li/AlN-LLZTO/LFP is significantly better than that of Li/LLZTO/LFP. After high-rate cycling, the Li/AlN-LLZTO/LFP recovers a discharge capacity of 131.1 mAh g^{-1} at 0.1 C. Figure 5d and Figure S9 show that the Li/AlN-LLZTO/LFP cell has the same charging and discharging platform as the typical LFP batteries that use a liquid electrolyte. Figure 5e (refer to S10 for details) shows the long-term cycling stability of the Li/AlN-LLZTO/LFP and Li/LLZTO/LFP cell at 0.2 C. As shown in Figure 5e, the Li/LLZTO/LFP cell has an initial charge and discharge capacity of 134.1 and 120.7 mAh g^{-1} with 90.0% coulomb efficiency, which is due to the poor interface contact between Li and the electrolyte. The cell-capacity decay-rate is fast during the cycle, and the capacity retention rate after 200 turns is only 49.3%. The cell, which is equipped with an AlN film, has an initial charge/discharge capacity of 144.7 and 134.5 mAh g^{-1}, with a Coulombic efficiency of 92.9%. The Coulombic efficiency was ~99% during the cycling, and the discharge specific capacity of the cell still had 122.6 mAh g^{-1} after 200 cycles, with a capacity retention rate of 93.1%. It can be seen that the cell with the AlN-modified layer has both a better rate performance and cycle performance than the cell without interface modification.

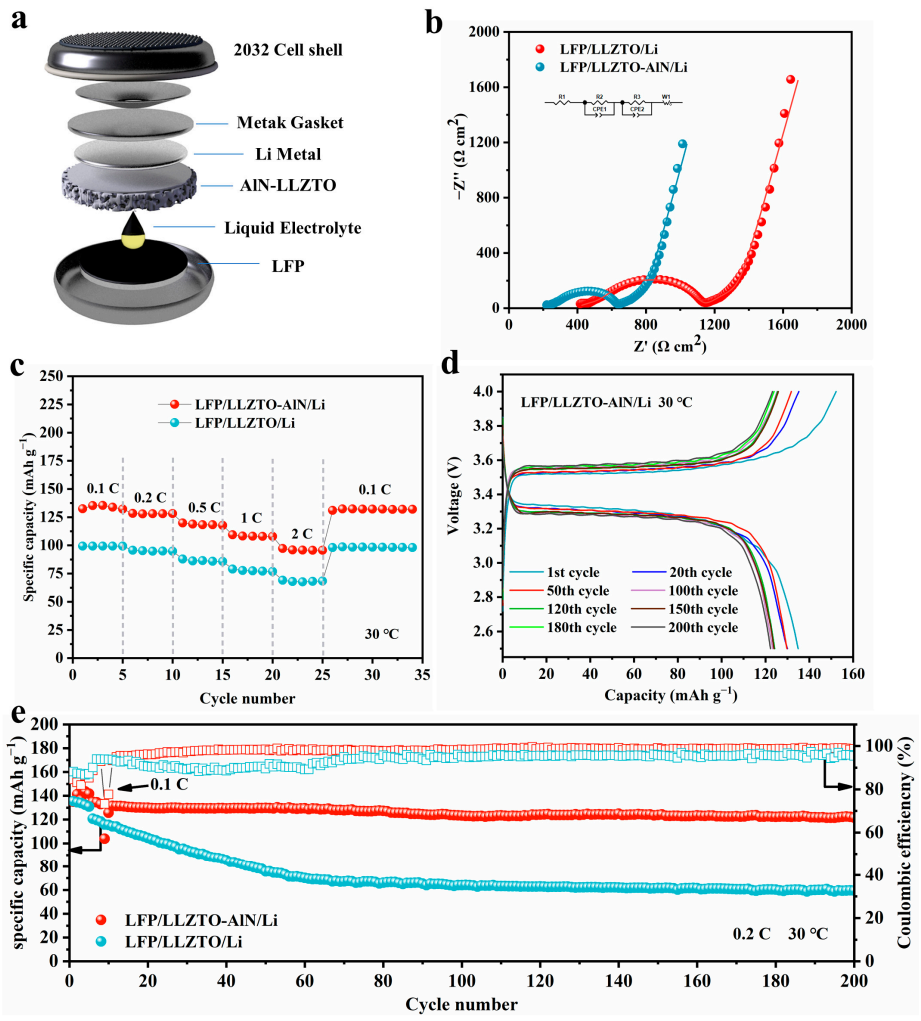

Figure 5. (**a**) Schematic configuration of the Li/AlN-LLZTO/LFP cell; (**b**) comparison of the EIS profiles of the cells using LLZTO with and without AlN modification; (**c**) rate performance of the Li/AlN-LLZTO/LFP cell; (**d**) the charge- and discharge-platform information for different cycles at 0.2 C; (**e**) long-term electrochemical performance of the Li/LLZTO/LFP, and the Li/AlN-LLZTO/LFP cell at 0.2 C.

The Li/AlN-LLZTO/LFP-containing AlN modified layer was further tested for cycling stability at high current-densities (at 0.5 C). As shown in Figure 6a, a current density of 0.1 C was used for initial activation during the initial 5 cycles, and it can be seen that the capacity of the battery is lower at high current-densities. The initial charge and discharge capacities of the Li/LLZTO/LFP battery at 0.5 C were 116.2 mAh g^{-1} and 115.1 mAh g^{-1}, respectively, and the coulombic efficiency during cycling was close to 100%. The specific discharge capacity of the battery was still 103.4 mAh g^{-1} after 80 cycles, with a capacity retention rate of 89.8%. Figure 6b shows the charging and discharging plateaus of the battery for different numbers of cycles. The results indicate that the introduction of the AlN layer enables the construction of a stable Li-electrode/electrolyte interface, which facilitates the transport of Li-ions between Li electrode and electrolyte and improves the performance of the full cells.

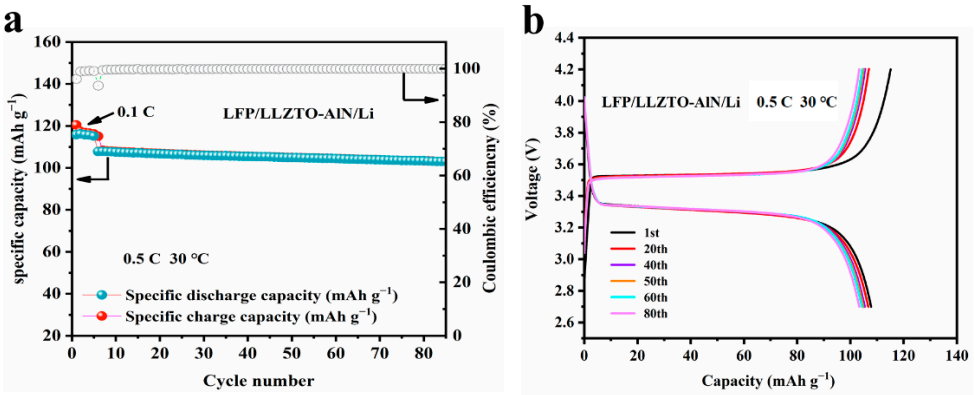

Figure 6. (**a**) Cycle performance of the Li/AlN-LLZTO/LFP cell at 0.5 C current density; (**b**) charge/discharge plateau of the Li/AlN-LLZTO/LFP at 0.5 C.

4. Conclusions

In this study, we synthesized cubic-phase LLZTO using a secondary sintering method and proposed an effective method to improve the wettability for the solid electrolyte of LLZTO on lithium, using an AlN interlayer. Theoretical calculations show that AlN has a high affinity for Li, while AlN is also wettable for LLZTO. The mutually wettable interface facilitates the diffusion of ions. The AlN film can ensure tight contact of the Li-metal/LLZTO interface and promote Li-ion transport. The assembled symmetric Li cells can cycle stably for 3600 h. The hybrid solid-state battery with the modified layer, which was assembled using $LiFePO_4$ (LFP), still had a capacity of 120 mAh g^{-1} after 200 cycles and a capacity retention rate of 98%. This suggests a satisfactory capacity and excellent cycle stability. This also shows that the introduction of an AlN interlayer is a very effective method to produce a stable Li-electrode/solid electrolyte interface and to improve the cycling stability of the battery.

Supplementary Materials: The following supporting information can be downloaded at: https://www.mdpi.com/article/10.3390/nano12122023/s1, Figure S1: The X-ray characteristics of AlN as a commercial reactant. Figure S2: Cross-sectional SEM image of the LLZTO pellet. Figure S3: The Nyquist curves of LLZTO at 25 °C. Figure S4: EIS spectra of LLZTO pellets with Ag as blocking electrodes at different temperatures in the range 25~60 °C. The insets show the equivalent circuit for thus obtained EIS results. Figure S5: DFT calculations of interfacial formation energies of Li/LLZTO Li/AlN and AlN/LLZTO. Figure S6: (a) Critical current density of Li/ LLZTO/Li (b) Critical current density of Li/AlN-LLZTO/Li. Figure S7: Voltage profiles and details for the Li/LLZTO/Li symmetric cell at current densities of 0.01 mA cm^{-2} with 0.005 mAh cm^{-2}. Figure S8: The charge and discharge platform information under different cycles at 0.2 C. Figure S9: (a) The long-term electrochemical performance of the Li/LLZTO/LFP cell under 0.2 C; (b) The long-term electrochemical performance of the Li/AlN-LLZTO/LFP cell under 0.2 C. Table S1: The conductivity data and resistances of LLZTO pellets with Ag as blocking electrodes at different temperatures in the range 25~60 °C.

Table S2: Nyquist plots fitted data for lithium symmetric cells. Table S3: Nyquist plots fitted data for hybrid solid-state full cells.

Author Contributions: Conceptualization, L.Z. and K.P.; methodology, W.Z., L.Z. and W.J.; software, S.L.; validation, L.D., S.Z. and B.A.; formal analysis, B.A.; investigation, L.D.; resources, K.P.; data curation, W.J.; writing—original draft preparation, W.J. and B.A.; writing—review and editing, W.J.; visualization, W.J. and L.D.; supervision, L.Z. and K.P.; All authors have read and agreed to the published version of the manuscript.

Funding: This research was funded by the National Natural Science Foundation of China (51574160, 21776175), National Key Research and Development Program of China (2017YFB0102004), Shandong Province National Natural Science Foundation (ZR2014EEM049), Key Research and Development Program of Shandong Province (2017CSGC0502, 2017GGX40102), Leading Talents Project: Science and Technology Talents and Platform Plan-training of Science and Technology Talent (2017HA012), and State Key Laboratory of Pressure Hydrometallurgical Technology of Associated Nonferrous Metal Resources (yy20160010).

Data Availability Statement: Data presented in this article are available on request from the corresponding author.

Acknowledgments: We thank the anonymous referee for the helpful comments and constructive remarks on this manuscript.

Conflicts of Interest: The authors declare no conflict of interest.

References

1. Cheng, X.B.; Zhang, R.; Zhao, C.Z.; Zhang, Q. Toward safe lithium metal anode in rechargeable batteries: A Review. *Chem. Rev.* **2017**, *117*, 10403–10473. [CrossRef] [PubMed]
2. Zhao, N.; Khokhar, W.; Bi, Z.; Shi, C.; Guo, X.; Fan, L.-Z.; Nan, C.-W. Solid garnet batteries. *Joule* **2019**, *3*, 1190–1199. [CrossRef]
3. Tarascon, J.M.; Armand, M. Issues and challenges facing rechargeable lithium batteries. In *Materials for Sustainable Energy*; Nature Publishing Group: Berlin, Germany, 2011; pp. 171–179.
4. Grey, C.P.; Tarascon, J.M. Sustainability and in situ monitoring in battery development. *Nat. Mater.* **2016**, *16*, 45–56. [CrossRef] [PubMed]
5. Chen, X.; He, W.; Ding, L.X.; Wang, S.; Wang, H. Enhancing interfacial contact in all solid-state batteries with a cathode-supported solid electrolyte membrane framework. *Energy Environ. Sci.* **2019**, *12*, 938–944. [CrossRef]
6. Bi, Z.; Li, X.; Chen, Y.; He, X.; Xu, X.; Gao, X. Large-scale multifunctional electrochromic-energy storage device based on tungsten trioxide monohydrate nanosheets and prussian white. *ACS Appl. Mater. Interfaces* **2017**, *9*, 29872–29880. [CrossRef]
7. Wang, C.; Zhang, L.; Xie, H.; Pastel, G.; Dai, J.; Gong, Y.; Liu, B.; Wachsman, E.D.; Hu, L. Mixed ionic-electronic conductor enabled effective cathode-electrolyte interface in all solid-state batteries. *Nano Energy* **2018**, *50*, 393–400. [CrossRef]
8. Jia, M.; Zhao, N.; Bi, Z.; Fu, Z.; Xu, F.; Shi, C.; Guo, X. Polydopamine-coated garnet particles homogeneously distributed in poly (propylene carbonate) for the conductive and stable membrane electrolytes of solid lithium batteries. *ACS Appl. Mater. Interfaces* **2020**, *12*, 46162–46169. [CrossRef]
9. Zhong, S.W.; Liang, T.X.; Yao, W.L.; Liu, X.L.; Lai, H.; Lei, C.; Li, D. Recent advancements in interface between cathode and garnet solid electrolyte for all solid-state Li-ion batteries. *J. Inorg. Mater.* **2019**, *34*, 694.
10. Zeng, X.X.; Yin, Y.X.; Li, N.W.; Du, W.C.; Guo, Y.G.; Wan, L.J. Reshaping lithium plating/stripping behavior via bifunctional polymer electrolyte for room-temperature solid li metal batteries. *J. Am. Chem. Soc.* **2016**, *138*, 15825–15828. [CrossRef]
11. Xu, K. Nonaqueous liquid electrolytes for lithium-based rechargeable batteries. *Chem. Rev.* **2003**, *104*, 4303–4418. [CrossRef]
12. Sun, Q.; Chen, X.; Xie, J.; Xu, X.; Tu, J.; Zhang, P.; Zhao, X. Nonflammable quasi-solid-state electrolyte for stable lithium-metal batteries. *RSC Adv.* **2019**, *9*, 42183–42193. [CrossRef] [PubMed]
13. Chinnam, P.R.; Wunder, S.L. Self-assembled janus-like multi-ionic lithium salts form nano-structured solid polymer electrolytes with high ionic conductivity and Li^+ ion transference number. *J. Mater. Chem. A* **2013**, *1*, 1731–1739. [CrossRef]
14. Goodenough, J.B.; Kim, Y. Challenges for rechargeable Li batteries. *Chem. Mater.* **2009**, *22*, 587–603. [CrossRef]
15. Goodenough, J.B.; Park, K.S. The Li-ion rechargeable battery: A perspective. *J. Am. Chem. Soc.* **2013**, *135*, 1167–1176. [CrossRef]
16. Subramanian, K.; Alexander, G.V.; Karthik, K.; Patra, S.; Indu, M.S.; Sreejith, O.V.; Viswanathan, R.; Narayanasamy, J.; Murugan, R. A brief review of recent advances in garnet structured solid electrolyte-based lithium metal batteries. *J. Energy Storage* **2021**, *33*, 102157. [CrossRef]
17. Li, S.; Zhang, S.Q.; Shen, L.; Liu, Q.; Ma, J.B.; Lv, W.; He, Y.B.; Yang, Q.H. Progress and perspective of ceramic/polymer composite solid electrolytes for lithium batteries. *Adv. Sci.* **2020**, *7*, 1903088. [CrossRef]
18. Yue, L.; Ma, J.; Zhang, J.; Zhao, J.; Dong, S.; Liu, Z.; Cui, G.; Chen, L. All solid-state polymer electrolytes for high-performance lithium-ion batteries. *Energy Storage Mater.* **2016**, *5*, 139–164. [CrossRef]
19. Arya, A.; Sharma, A.L. Polymer electrolytes for lithium-ion batteries: A critical study. *Ionics* **2017**, *23*, 497–540. [CrossRef]

20. Liang, Y.F.; Xia, Y.; Zhang, S.Z.; Wang, X.L.; Xia, X.H.; Gu, C.D.; Wu, J.B.; Tu, J.P. A preeminent gel blending polymer electrolyte of poly (vinylidene fluoride-hexafluoropropylene) -poly (propylene carbonate) for solid-state lithium ion batteries. *Electrochim. Acta* **2019**, *296*, 1064–1069. [CrossRef]
21. Langer, F.; Bardenhagen, I.; Glenneberg, J.; Kun, R. Microstructure and temperature dependent lithium-ion transport of ceramic-polymer composite electrolyte for solid-state lithium-ion batteries based on garnet-type $Li_7La_3Zr_2O_{12}$. *Solid State Ion.* **2016**, *291*, 8–13. [CrossRef]
22. Long, L.; Wang, S.; Xiao, M.; Meng, Y. Polymer electrolytes for lithium polymer batteries. *J. Mater. Chem. A* **2016**, *4*, 10038–10069. [CrossRef]
23. Xue, Z.; He, D.; Xie, X. Poly (ethylene oxide)-based electrolytes for lithium-ion batteries. *J. Mater. Chem. A* **2015**, *3*, 19218–19253. [CrossRef]
24. Shaplov, A.S.; Marcilla, R.; Mecerreyes, D. Recent advances in innovative polymer electrolytes based on polys (ionic liquid). *Electrochim. Acta* **2015**, *175*, 18–34. [CrossRef]
25. Zhou, D.; Shanmukaraj, D.; Tkacheva, A.; Armand, M.; Wang, G. Polymer electrolytes for lithium-based batteries: Advances and prospects. *Chem* **2019**, *5*, 2326–2352. [CrossRef]
26. Lacivita, V.; Westover, A.S.; Kercher, A.; Phillip, N.D.; Yang, G.; Veith, G.; Ceder, G.; Dudney, N.J. Resolving the amorphous structure of lithium phosphorus oxynitride (lipon). *J. Am. Chem. Soc.* **2018**, *140*, 11029–11038. [CrossRef]
27. Sepúlveda, A.; Criscuolo, F.; Put, B.; Vereecken, P.M. Effect of high temperature LiPON electrolyte in all solid-state batteries. *Solid State Ion.* **2019**, *337*, 24–32. [CrossRef]
28. Fang, H.; Jena, P. Li-rich antiperovskite superionic conductors based on cluster ions. *Proc. Natl. Acad. Sci. USA* **2017**, *114*, 11046–11051. [CrossRef]
29. Zhang, J.; Zheng, C.; Lou, J.; Xia, Y.; Liang, C.; Huang, H.; Gan, Y.; Tao, X.; Zhang, W. Poly (ethylene oxide) reinforced Li_6PS_5Cl composite solid electrolyte for all-solid-state lithium battery: Enhanced electrochemical performance, mechanical property and interfacial stability. *J. Power Source* **2019**, *412*, 78–85. [CrossRef]
30. Thangadurai, V.; Narayanan, S.; Pinzaru, D. Garnet-type solid-state fast Li ion conductors for Li batteries: Critical review. *Chem. Soc. Rev.* **2014**, *43*, 4714–4727. [CrossRef]
31. Su, Y.; Falgenhauer, J.; Polity, A.; Leichtweiß, T.; Kronenberger, A.; Obel, J.; Zhou, S.; Schlettwein, D.; Janek, J.; Meyer, B.K. LiPON thin films with high nitrogen content for application in lithium batteries and electrochromic devices prepared by RF magnetron sputtering. *Solid State Ion.* **2015**, *282*, 63–69. [CrossRef]
32. Wolfenstine, J.; Allen, J.L.; Sumner, J.; Sakamoto, J. Electrical and mechanical properties of hot-pressed versus sintered $LiTi_2(PO_4)_3$. *Solid State Ion.* **2009**, *180*, 961–967. [CrossRef]
33. Catti, M. Local structure of the $Li_{1/8}La_{5/8}TiO_3$ (LLTO) ionic conductor by theoretical simulations. *J. Phys. Conf. Ser.* **2008**, *117*, 012008. [CrossRef]
34. Mizuno, F.; Hayashi, A.; Tadanaga, K.; Tatsumisago, M. High lithium ion conducting glass-ceramics in the system Li_2S–P_2S_5. *Solid State Ion.* **2006**, *177*, 2721–2725. [CrossRef]
35. Saienga, J.; Martin, S.W. The comparative structure, properties, and ionic conductivity of LiI+Li_2S+GeS_2 glasses doped with Ga_2S_3 and La_2S_3. *J. Non-Cryst. Solids* **2008**, *354*, 1475–1486. [CrossRef]
36. Manthiram, A.; Yu, X.; Wang, S. Lithium battery chemistries enabled by solid-state electrolytes. *Nat. Rev. Mater.* **2017**, *2*, 1–16. [CrossRef]
37. Awaka, J.; Kijima, N.; Hayakawa, H.; Akimoto, J. Synthesis and structure analysis of tetragonal $Li_7La_3Zr_2O_{12}$ with the garnet-related type structure. *J. Solid State Chem.* **2009**, *182*, 2046–2052. [CrossRef]
38. Gao, K.; He, M.; Li, Y.; Zhang, Y.; Gao, J.; Li, X.; Cui, Z.; Zhan, Z.; Zhang, T. Preparation of high-density garnet thin sheet electrolytes for all-solid-state Li-metal batteries by tape-casting technique. *J. Alloys Compd.* **2019**, *791*, 923–928. [CrossRef]
39. Zhao, N.; Fang, R.; He, M.H.; Chen, C.; Li, Y.Q.; Bi, Z.J.; Guo, X.X. Cycle stability of lithium/garnet/lithium cells with different intermediate layers. *Rare Met.* **2018**, *37*, 473–479. [CrossRef]
40. Flatscher, F.; Philipp, M.; Ganschow, S.; Wilkening, H.M.R.; Rettenwander, D. The natural critical current density limit for $Li_7La_3Zr_2O_{12}$ garnets. *J. Mater. Chem. A* **2020**, *8*, 15782–15788. [CrossRef]
41. Fu, K.K.; Gong, Y.; Fu, Z.; Xie, H.; Yao, Y.; Liu, B.; Carter, M.; Wachsman, E.; Hu, L. Transient behavior of the metal interface in lithium metal-garnet batteries. *Angew. Chem. Int. Ed. Engl.* **2017**, *56*, 14942–14947. [CrossRef]
42. Luo, W.; Gong, Y.; Zhu, Y.; Li, Y.; Yao, Y.; Zhang, Y.; Fu, K.K.; Pastel, G.; Lin, C.F.; Mo, Y.; et al. Reducing interfacial resistance between garnet-structured solid-state electrolyte and li-metal anode by a germanium layer. *Adv. Mater.* **2017**, *29*, 1606042. [CrossRef] [PubMed]
43. Wang, C.; Xie, H.; Zhang, L.; Gong, Y.; Pastel, G.; Dai, J.; Liu, B.; Wachsman, E.D.; Hu, L. Universal soldering of lithium and sodium alloys on various substrates for batteries. *Adv. Energy Mater.* **2017**, *8*, 1701963. [CrossRef]
44. Chengwei, W.; Gong, Y.; Liu, B.; Fu, K.; Yao, Y.; Hitz, E.; Li, Y.; Dai, J.; Xu, S.; Luo, W.; et al. Conformal, Nanoscale ZnO surface modification of garnet-based solid-state electrolyte for lithium metal anodes. *Nano Lett.* **2017**, *17*, 565–571.
45. Chen, Y.; He, M.; Zhao, N.; Fu, J.; Huo, H.; Zhang, T.; Li, Y.; Xu, F.; Guo, X. Nanocomposite intermediate layers formed by conversion reaction of SnO_2 for Li/garnet/Li cycle stability. *J. Power Source* **2019**, *420*, 15–21. [CrossRef]
46. Sudo, R.; Nakata, Y.; Ishiguro, K.; Matsui, M.; Hirano, A.; Takeda, Y.; Yamamoto, O.; Imanishi, N. Interface behavior between garnet-type lithium-conducting solid electrolyte and lithium metal. *Solid State Ion.* **2014**, *262*, 151–154. [CrossRef]

47. Han, X.; Gong, Y.; Fu, K.K.; He, X.; Hitz, G.T.; Dai, J.; Pearse, A.; Liu, B.; Wang, H.; Rubloff, G.; et al. Negating interfacial impedance in garnet-based solid-state Li metal batteries. *Nat. Mater.* **2017**, *16*, 572–579. [CrossRef]
48. Motoyama, M.; Tanaka, Y.; Yamamoto, T.; Tsuchimine, N.; Kobayashi, S.; Iriyama, Y. The Active Interface of Ta-doped $Li_7La_3Zr_2O_{12}$ for Li plating/stripping revealed by acid aqueous etching. *ACS Appl. Energy Mater.* **2019**, *2*, 6720–6731. [CrossRef]
49. Ma, C.; Rangasamy, E.; Liang, C.; Sakamoto, J.; More, K.L.; Chi, M. Excellent stability of a lithium-ion-conducting solid electrolyte upon reversible Li^+/H^+ exchange in aqueous solutions. *Angew. Chem. Int. Ed. Engl.* **2015**, *54*, 129–133. [CrossRef]
50. Sharafi, A.; Kazyak, E.; Davis, A.L.; Yu, S.; Thompson, T.; Siegel, D.J.; Dasgupta, N.P.; Sakamoto, J. Surface chemistry mechanism of ultra-low interfacial resistance in the solid-state electrolyte $Li_7La_3Zr_2O_{12}$. *Chem. Mater.* **2017**, *29*, 7961–7968. [CrossRef]
51. Rettenwander, D. One step closer to realizing solid-state batteries with cubic $Li_7La_3Zr_2O_{12}$ garnets. *Chem* **2019**, *5*, 1695–1696. [CrossRef]
52. Peng, Z.; Ren, F.; Yang, S.; Wang, M.; Sun, J.; Wang, D.; Xu, W.; Zhang, J.G. A highly stable host for lithium metal anode enabled by Li_9Al_4-Li_3N-AlN structure. *Nano Energy* **2019**, *59*, 110–119. [CrossRef]
53. Kresse, G.; Furthmüller, J. Efficiency of ab-initio total energy calculations for metals and semiconductors using a plane-wave basis set. *Comput. Mater. Sci.* **1996**, *6*, 15–50. [CrossRef]
54. Perdew, J.P.; Burke, K.; Ernzerhof, M. Generalized gradient approximation made simple. *Phys. Rev. Lett.* **1996**, *77*, 3865–3868. [CrossRef] [PubMed]
55. Kresse, G.; Furthmüller, J. Efficient iterative schemes for ab initio total-energy calculations using a plane-wave basis set. *Phys. Rev. B* **1996**, *54*, 11169. [CrossRef] [PubMed]
56. Kresse, G.; Joubert, D. From ultrasoft pseudopotentials to the projector augmented-wave method. *Phys. Rev. B* **1999**, *59*, 1758–1775. [CrossRef]
57. Tietz, F.; Wegener, T.; Gerhards, M.T.; Giarola, M.; Mariotto, G. Synthesis and raman micro-spectroscopy investigation of $Li_7La_3Zr_2O_{12}$. *Solid State Ion.* **2013**, *230*, 77–82. [CrossRef]
58. Larraz, G.; Orera, A.; Sanjuán, M.L. Cubic phases of garnet-type $Li_7La_3Zr_2O_{12}$: The role of hydration. *J. Mater. Chem. A* **2013**, *1*, 11419–11428. [CrossRef]
59. David, I.N.; Thompson, T.; Wolfenstine, J.; Allen, J.L.; Sakamoto, J.; Viyas, B. Microstructure and Li-ion conductivity of hot-pressed cubic $Li_7La_3Zr_2O_{12}$. *J. Am. Ceram. Soc.* **2015**, *98*, 1209–1214. [CrossRef]
60. Li, Y.; Chen, X.; Dolocan, A.; Cui, Z.; Xin, S.; Xue, L.; Xu, H.; Park, K.; Goodenough, J.B. Garnet electrolyte with an ultralow interfacial resistance for Li-metal batteries. *J. Am. Chem. Soc.* **2018**, *140*, 6448–6455. [CrossRef]
61. Ruan, Y.; Lu, Y.; Huang, X.; Su, J.; Sun, C.; Jin, J.; Wen, Z. Acid induced conversion towards a robust and lithiophilic interface for Li–$Li_7La_3Zr_2O_{12}$ solid-state batteries. *J. Mater. Chem. A* **2019**, *7*, 14565–14574. [CrossRef]